RSC Advances

PAPER

View Article Online
View Journal | View Issue

Cite this: *RSC Adv.*, 2025, **15**, 19884

Deep eutectic solvent-assisted carbon quantum dots for nanomolar detection of 4-nitrophenol†

Mandeep Kaur, Mily Bhattacharya * and Banibrata Maity *

4-Nitrophenol (4-NP) is a toxic, persistent, and carcinogenic pollutant, classified by the U.S. EPA as a primary contaminant. Commonly released by the pharmaceutical industry, it poses serious health risks, damaging the liver, kidneys, central nervous system, and bloodstream, highlighting the need for eco-friendly detection methods. To solve the difficulty of 4-NP detection, the work offers a unique and sustainable detection approach based on nitrogen and chlorine co-functionalized carbon quantum dots (S-CQDs). The hydrothermal approach was used for the synthesis, with sucrose serving as a carbon precursor and a deep eutectic solvent (DES) composed of urea and choline chloride in a 1 : 2 molar ratio. The nanosensor exhibited strong green fluorescence, excellent water solubility, photostability and ~56%. Quantum yield. HRTEM revealed spherical and monodispersed S-CQDs that averaged 3.06 nm in size. FTIR and XPS investigations revealed amino, hydroxyl, carboxyl, and chlorine groups on the surface of S-CQDs, confirming intrinsic nitrogen and chlorine functionalization. XRD, UV-vis spectroscopy, fluorescence spectroscopy, and TCSPC were used for further characterization. For 4-nitrophenol (4-NP), the nanoprobe demonstrated excellent sensitivity and selectivity with a detection limit of 10 nM. An inner filter effect (IFE) associated with a zwitterionic spirocyclic Meisenheimer complex was confirmed by mechanistic investigations because of spectrum overlap and unaltered lifespan values. To further elucidate the sensing process, photophysical metrics like binding constants and quenching efficiency were also assessed. This work paves the way for developing a sensitive, green fluorescent nanosensor for a rapid, cost-effective and environmentally friendly approach as well as on-site detection of 4-NP, offering a promising tool for pollution monitoring and control for environmental water samples.

Received 4th February 2025
Accepted 4th June 2025

DOI: 10.1039/d5ra00824g

rsc.li/rsc-advances

1. Introduction

Hazardous organic pollutants such as 4-nitrophenol (4-NP) are released into the environment as a result of industrial and agricultural operations. 4-NP is dangerous and difficult to detect, even at low quantities. It is utilized in the manufacturing of leather goods, pigments, and medications. 4-NP can damage aquatic life, disturb microbial ecosystems, induce cancer in animals, and put humans in a coma or poison them even at low concentrations. The U.S. EPA restricts its content in drinking water to 0.43 μM L^{-1} because of its toxicity and environmental persistence. Thus, it is crucial to create a sensitive and precise technique for identifying 4-NP.[1–4]

In the realm of nanotechnology, carbon quantum dots (CQDs) are very versatile due to their distinct optical, electrical, and chemical capabilities. These sub-10 nm carbon particles with crystalline or partially amorphous cores and functional surface groups outperform standard dyes and semiconductor quantum dots.[5,6] Their low toxicity, biocompatibility, low cost, and high photostability make them ideal for use in optoelectronics, energy conversion, photocatalysis, sensing, bioimaging, cell labeling, and drug delivery. As a result, CQDs

Department of Chemistry and Biochemistry, Thapar Institute of Engineering and Technology, Patiala 147004, India. E-mail: mily.bhattacharya@thapar.edu; banibrata.maity@thapar.edu

† Electronic supplementary information (ESI) available: Fig. S1 displays schematic representation of interactions between choline chloride and urea to form deep eutectic solvent (DES), schematic representation of synthetic protocol of DES from choline chloride and urea. Fig. S2 depicts energy dispersive spectroscopy (EDS) spectrum of S-CQDs demonstrating the presence of numerous elements on S-CQDs surface. Fig. S3 depicts S-CQDs fluorescence emission spectra for optimization of the reaction time, volume ratio and zeta potential plot. Fig. S4 displays variation in fluorescence emission of S-CQDs in the presence of different concentrations of 4-NP (0–3.8 μM) where black arrow depicts the progressive decrease of fl. Intensity of S-CQDs, the spectra depicting linear correlation between $F_0 - F/F_0$ and different concentrations of 4-NP (0 to 0.38 μM), (inset) linear correlation between $F_0 - F/F_0$ and some specific concentrations of 4-NP (0 to 0.56 μM), and fluorescence lifetime decays of S-CQDs. Fig. S5 depicts interference studies of S-CQDs-4-NP interaction in the presence of various metal ions, and biomolecules. Fig. S6 displays (a) FTIR spectra of DES, (b) combined FTIR spectra of DES, S-CQDs and S-CQDs-4-NP complex. Fig. S7 shows Stern–Volmer plot of S-CQDs in aqueous medium, and real sample of 4-NP. Fig. S8 displays Benesi–Hildebrand plot of S-CQDs in aqueous medium, and real sample of 4-NP. Table S2 includes fluorescence lifetime components of S-CQDs and their respective coefficients along with the mean fluorescence lifetimes. Table S3 represents implementation of the synthesized nanosensor for detection of real sample of 4-NP in river water. See DOI: https://doi.org/10.1039/d5ra00824g

have been a fast developing focus of scientific and industrial research.[7]

Bottom-up procedures, such as carbonizing glucose, glycol, ascorbic acid, and other chemicals, are commonly employed to create luminous carbon dots (C-dots). However, most synthesis methods include numerous stages, strong acids, and surface passivation to improve water solubility and luminescence. To manufacture self-passivated, photoluminescent C-dots, a simple, one-step, cost-effective method is required. Hydrothermal carbonization provides such a process, which is low-cost, environmentally benign, and nontoxic, and can use a variety of precursors.[8]

Deep eutectic solvents (DESs) are novel, environmentally benign, low-cost, and recyclable solvents with good solubility and biocompatibility.[9,10] Because of their rich elemental composition, they are excellent solvents and doping agents for the synthesis of doped carbon dots (CDs).[11,12] DESs are created by combining hydrogen bond acceptors (HBAs), such as quaternary ammonium compounds, and hydrogen bond donors (HBDs), such as acids, alcohols, or amines, resulting in a eutectic mixture with a lower melting point than the separate components.[13] Changing the HBAs, HBDs, or surface functionalization can affect the CDs' sensing and emission capabilities. Thus, DESs were used in this study for both doping and solvent functions in CD manufacture.[14] Shein *et al.* discuss the increasing popularity of DESs in the synthesis, functionalization, and use of biomass-derived carbonaceous materials (BCMs). Overall, using designer DESs to prepare and functionalize BCMs can help to develop long-lasting and cost-effective technologies for a variety of applications.[15] Wang *et al.* demonstrated the production of unique dual-functional carbon dots (N/Cl-CDs) in a choline chloride–glycerine deep eutectic solvent for selective sensing of intracellular pH and cyt-c levels *via* cell imaging.[16] Tang *et al.* suggested a novel strategy for the green production of CDs using DES treatment of lignocellulose and used it for the metal ions detection, with a detection limit of 191 ppm for Fe^{3+}. CDs have also proven to be useful for applications such as data storage and anti-counterfeit encryption.[17] Ten carbon dots were created by Tabaraki *et al.* using deep eutectic solvents based on choline chloride. The characteristics and doping of the CD were found to be controlled by the hydrogen bond donor's (HBD) molecular structure.[18]

There are several methods for synthesizing carbon quantum dots (CQDs), but employing sucrose, *i.e.* inexpensive, plentiful, and biodegradable material as a precursor provides a sustainable and cost-effective solution.[19] Saccharide-based CDs enable green synthesis and have applications in sensing, photocatalysis, and drug administration. Sucrose was chosen for its substantial amount of carbon (sp^2 and sp^3 carbons) and oxygen-containing functional groups such as hydroxyl, epoxy, and carbonyl.[20–22] This work investigates the synthesis, characteristics, and uses of sucrose-derived CQDs. In aqueous solution, sucrose hydrolyzes to fructose and glucose, which breakdown into smaller organics such as furfurals and weak acids. These polymerize following hydrothermal treatment to create CQDs.[23–25] Choline chloride (ChCl) & urea are two of the most extensively researched deep eutectic solvents (DES). Abbott *et al.* discovered that a 1 : 2 molar ratio of ChCl to urea produces a eutectic combination with a melting point of 12 °C, which is substantially lower than the respective melting temperatures of ChCl (302 °C) and urea (133 °C), making it acceptable as an ambient temperature solvent.[26] This DES has demonstrated outstanding effectiveness in catalytic processes, organic synthesis, electrochemistry, and nanoparticles generation.[27–31] We produced a green DES using ChCl and urea for the synthesis of carbon quantum dots (S-CQDs), which were then used as a nanosensor. Because of their low toxicity, biodegradability, affordability, and ease of manufacture, DESs are seen as environmentally acceptable, long-term alternatives to traditional solvents. They provide functional groups such as N and Cl to aid in S-CQD functionalization. Amide linkages in the DES also help to produce zwitterionic spirocyclic Meisenheimer complexes (Scheme 2), which promote energy transfer between S-CQDs and 4-NP, resulting in fluorescence quenching.[32–35]

Methods for detecting 4-NP include spectrophotometry, electrochemistry, chromatography, capillary electrophoresis, chemiluminescence, and fluorescence. However, many of these techniques are impracticable due to high costs, complex apparatus, time-consuming procedures, and the likelihood of producing harmful byproducts.[36,37] On the contrary, fluorescence spectrophotometry is frequently employed due to its ease of use, speed, excellent selectivity and sensitivity, and cheap operational cost.[38,39]

Peng *et al.* synthesized fluorescent sulfur quantum dots (SQDs) *via* top down approach using PEG and sublimed sulfur powder by stirring in oil bath for 72 h at 70 °C for detecting 4-NP with LOD 70 nM.[40] Tu *et al.* synthesized fluorescent nitrogen and phosphorus-doped carbon dots (Aa N,P-CDs) from Auricularia auricula *via* a hydrothermal method for detection of 4-nitrophenol (4-NP) with limit of detection 198 nM in a linear range of 0–37.5 μM.[41] Fang *et al.* discovered metal Cu-doped carbon dots (Cu-CDs) *via* single-step hydrothermal route (180 °C for 10 hours) as an effective method to detect *p*-NP with LOD 80 nM in the linear range of 0.5–50 μM.[42] Huang *et al.* reported the sensitive detection of 4-NP having 0.05 μM detection limit using cuttlefish ink-based N and S co-doped CQDs.[43] Amjadi and Hallaj studied a glucose-derived CQD–$Ru(bpy)_3^{2+}$–Ce(IV) chemiluminescence sensor designed for the determination of 4-NP.[44] Tian *et al.* reported synthesis of nitrogen-doped carbon dots (N-CDs) *via* hydrothermal method (200 °C for 9 hours) using *o*-phenylenediamine and dicyandiamine for 4-nitrophenol (4-NP) over a concentration range of 0.1–39 μM, corresponding to a detection limit (LOD) of 0.05 μM.[45] Soni *et al.* synthesized triflic acid treated palm shell based carbon quantum dots for successful 4-NP detection with limit of detection 0.079 μM with linearity in the range 0.2–0.40 μM.[46] Swain *et al.* synthesized and developed fluorescent N,S-CDs from a single natural precursor, the Giloy stem, using a hydrothermal technique, as well as an efficient fluorescent/colorimetric probe for the detection of organic contaminants congo red and 4-NP.[47] Yuan and colleagues have created a simple, environmentally friendly method for creating luminous N-CDs by the hydrothermal treatment of readily available, inexpensive maleic acid and ethylenediamine. The fluorescent

sensor recognizes 4-NP with good sensitivity and selectivity. The straightforward, quick, and dependable N-CDs sensor demonstrates how a CD-based platform may be used in the environmental monitoring industry.[48] Qu *et al.* used natural plant celery leaves as the starting material and glutathione as a S and N dopant to produce water-soluble CDs with good fluorescence qualities *via* a simple hydrothermal technique. These findings demonstrated that CDs have the potential to be used as fluorescent probes for detecting 2-NP, 3-NP, and 4-NP in environmental samples due to their rapid reaction, high specificity, and sensitivity.[49] Wang *et al.* created CQDs in a single-step using citric acid monohydrate as a carbon source and *o*-phenylenediamine as a surface modification. The developed carbon dot-imprinted fluorescence sensor encompasses a high 4-NP quenching efficiency. The results demonstrated that the fluorescence sensor has significant value for recognizing 4-NP in environmental samples.[1] Bogireddy *et al.* developed a simple technique for detecting 4-nitrophenol (4-NP) utilizing highly luminous nitrogen-doped oxidized carbon dots derived from citric acid and urea. Fluorescence quenching (switch OFF) with the addition of tiny quantities of organic pollutant (4-NP) has been linked to the total reduction of nitrogen-doped oxidized carbon dots (NOCDs) to reduced nitrogen-doped oxidized carbon dots (rNOCDs).[50]

S-CQDs were produced in a single step hydrothermal process with sucrose as the carbon source and ChCl-urea DES as a green solvent, N/Cl dopant, and passivating agent. The procedure is environmentally benign, avoids harsh chemicals, and achieves ultra-low nanomolar detection limits for 4-NP, exceeding many previously published methods (as shown in Table 3 and S1†). S-CQDs feature intense fluorescence, a spherical form, and excellent water solubility, making them ideal fluorescent nanoprobes for highly selective and sensitive on-site detection of 4-NP, a major industrial contaminant. This low-cost, long-term solution helps to further global water treatment projects by supporting safe water reuse and a healthier future.[51]

2. Experimental section

2.1. Materials

To prepare fluorescent S-CQDs sucrose, ascorbic acid (AA), and glucose were procured from HiMedia and used as obtained. Sodium citrate, sodium phosphate monobasic, trizma base, alanine (Ala), arginine (Arg), asparagine (Asn), aspartic acid (Asp), cysteine (Cys), glutamic acid (Glu), glutamine (Gln), histidine (His), isoleucine (Ile), leucine (Leu), lysine (Lys), methionine (Met), threonine (Thr), tryptophan (Trp), tyrosine (Tyr), valine (Val), were bought from Sigma Aldrich, India, and were employed without any additional purification. 4-Nitrophenol (4-NP), ferric chloride hexahydrate ($FeCl_3 \cdot 6H_2O$), manganese(II) chloride tetrahydrate ($MnCl_2 \cdot 3H_2O$), lead nitrate [$Pb(NO_3)_2$], potassium chloride (KCl), cobalt chloride hexahydrate ($CoCl_2 \cdot 6H_2O$), nickel(II) chloride hexahydrate ($NiCl_2 \cdot 6H_2O$), sodium chloride (NaCl), magnesium chloride hexahydrate ($MgCl_2 \cdot 6H_2O$), barium chloride dihydrate ($BaCl_2 \cdot 2H_2O$), sodium hydroxide pallets (NaOH), 3-NP, 2-NP, ferrous chloride ($FeCl_2$), hydrochloric acid (HCl), mercuric chloride ($HgCl_2$), picric acid, glutathione, quinine sulfate were purchased from Loba Chemie, India and employed without any additional purification. The pH of the buffers was adjusted with a pH meter (EUTECH pH/Ion 510) to a final value of ($\pm$0.02) at ~24–25 °C. All the investigation has been undertaken using double-distilled water. The 0.22 μM and 0.02 μM membrane filters were bought from Merck Millipore and Whatman (GE Healthcare Life Sciences), respectively. In order to assess the applicability of the current nanosensor, an experiment was carried out using real samples from river water. The water samples were obtained from local river in Patiala, Punjab, India. After spiking the river water sample with different concentrations 4-NP to the S-CQDs aqueous solution and fluorescence measurements were recorded at an excitation wavelength of 390 nm.

2.2. Synthesis of deep eutectic solvent (DES)

DES was synthesized from choline chloride (HBA) and urea (HBD). In a 100 mL beaker, 13.9 g of choline chloride and 12.8 g of urea were combined in a molar ratio of 1 : 2 (Fig. S1a†). The mixture was then heated at 80 °C while being continuously stirred for 30 minutes until a transparent and homogeneous liquid was formed (Fig. S1b†). The DES solvent was freshly synthesized every time for S-CQDs preparation and characterization and stored at room temperature (~24–25 °C).

2.3. Synthesis of S-CQDs

S-CQDs were synthesised using a hydrothermal synthesis technique. The sucrose aqueous solution (1 gram in 10 mL double-distilled water) along with 10 mL DES solution (Choline chloride and urea in 1 : 2) was transferred into an autoclave and the reaction was set up in a hydrothermal reactor at 200 °C for 2 hours. Carbonization changed the color from transparent to dark brown, suggesting the development of S-CQDs. After coming to the room temperature, the solution was centrifuged at 8000 rpm for 20 minutes and decanted. In order to further remove larger particles, the decanted solution was filtered *via* a 0.22 μm syringe filter and a 0.02 μm membrane filter respectively. The methodology for the synthesis of S-CQDs is depicted schematically below (Scheme 1). Finally, the brown colored S-CQDs solution was collected and stored in a refrigerator at 4 °C for future experimental investigations. Each time freshly synthesized S-CQDs were employed for the characterization and spectroscopic analyses.

2.4. Characterization of S-CQDs

2.4.1. Electron microscopy. High-resolution transmission electron microscopy (HRTEM) *via* JEM 2100 plus (JEOL) equipped with a charge-coupled device (CCD) camera at an acceleration voltage of 80–200 kV was used to characterize the synthesised S-CQDs. The samples were made by spreading a tiny droplet of diluted S-CQDs solution 1 : 1 (v/v) of S-CQDs and double distilled water over a copper grid and allowing it to dry overnight ~12–16 hours at room temperature (~24–25 °C). To determine the morphology and size of S-CQDs, HRTEM imaging is performed in a single session since it produces

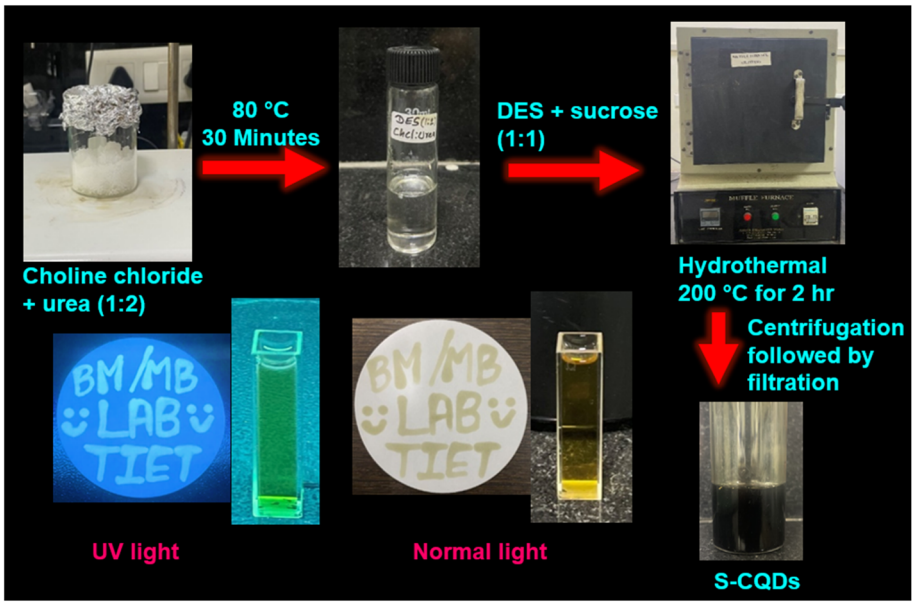

Scheme 1 Schematic representation of synthetic protocol of S-CQDs from Sucrose.

enough high-resolution images for reliable measurements and statistical analysis. For statistical analysis of HRTEM images, ImageJ and OriginPro 2021 software were used to generate size distribution histograms of S-CQDs, which were subsequently fitted with normal distribution curves.

2.4.2. X-ray photoelectron spectroscopy (XPS) and energy dispersive spectroscopy (EDS). The XPS survey spectra were collected using an Escalab Xi$^+$ X-ray photoelectron spectrometer from Thermo Fisher Scientific (USA). XPS is performed in single session. The spectra were first baseline corrected, and then the peaks were identified using the peak analyzer feature and deconvoluted *via* multiple peak-fitting employing the Gaussian function, both of which are included in the OriginPro 2021 software. The deconvoluted peaks were best fit using a correlation coefficient (R^2) of 0.99. The energy-dispersive spectroscopy (EDS) of S-CQDs was measured using the Bruker QUANTAX 200 from ZEISS Sigma.

2.4.3. Grazing-incidence X-ray diffraction (GIXRD). S-CQDs diffraction pattern was captured on Rigaku SmartLab with a 2θ angular range of 10–90°. The scan pace was 3.02 degrees/minute, and the scan resolution was 0.0001 degrees. Three replicates were performed for the experiment.

2.4.4. Attenuated total reflectance fourier-transform IR (ATR FT-IR) spectroscopy. The ATR-FTIR spectra of the S-CQDs were acquired using an IRTracer-100 spectrophotometer (Shimadzu) equipped with the QATRTM single-reflection integration-type ATR accessory, comprising a diamond crystal, and an air-cooled DLATGS detector. A resolution of 2 cm^{-1} was preserved while capturing all spectra in transmittance mode. The final spectrum was an average of 100 scans. Before putting a sample drop on the crystal, methanol was used to clean the surface and background scan with 100 accumulations was run prior to recording spectrum. 10 μL sample drop was utilized to acquire spectra within the range 400–4000 cm^{-1}. The experiment was performed thrice and the spectral data was replotted using OriginPro 2021.

2.4.5. UV-visible spectroscopy and zeta potential (ζ) measurements. The UV-vis absorption spectra of S-CQD aqueous solutions were obtained using a quartz cuvette having a path length of 1 cm using a UV-vis spectrophotometer (Shimadzu, RF-2600). To record the absorbance, 100 μL of the S-CQDs solution was added in double-distilled water to a total volume of 3 mL. The S-CQDs zeta potential was measured using a Brookhaven 90 Plus zeta potential analyzer. Three replicates were carried out for both techniques.

2.4.6. Preparation of S-CQDs sample for fluorescence studies. 30 μL of the synthesised S-CQDs was added to 2.47 mL of double-distilled water to achieve a total amount of 2.5 mL. During the fluorescence emission measurements, the volume of S-CQDs was held constant while the concentration of 4-nitrophenol (4-NP) varied (0–3.8 μM) with an excitation wavelength of 390 nm.

2.4.7. Steady state fluorescence spectroscopy. The Shimadzu RF-6000 spectrofluorometer was used to acquire the fluorescence spectra of S-CQDs. S-CQD fluorescence spectra was collected at λ_{ex} = 390 nm with a scan range of 392–680 nm. Emission and excitation bandwidths were set at 5 and 10 nm respectively. Further to determine the limit of detection, binding constant, and Stern–Volmer quenching constant (K_{S-V}), the emission intensities were fitted using a linear equation found in the OriginPro 2021 as indicated below:

$$y = a + bx \quad (1)$$

The fluorescence intensity ratio, or F_0/F, is represented by the variable y, where the parameters "F_0" and "F" denote the fluorescence intensity in the presence and absence of 4-NP, respectively. The intercept is denoted by "a," the slope by "b,"

and the quencher concentration (4-NP) by "x". Every steady-state fluorescence experiment was repeated at least three times. Error bars represent standard error of measurements obtained from three independent experiments. All the steady state fluorescence experiments were repeated three times.

2.4.8. Photoluminescence quantum yield (PLQY) measurements. The photoluminescence quantum yield (PLQY) of S-CQDs was determined using quinine sulphate in 0.1 M H_2SO_4 as a standard reference solution (quantum yield 0.546).[52] The following equation was used to determine the PLQY values:[53]

$$\phi_S = \phi_R \times \frac{A_S}{A_R} \times \frac{(Abs)_R}{(Abs)_S} \times \frac{{\eta_S}^2}{{\eta_R}^2} \quad (2)$$

The parameters 'ϕ_S' and 'ϕ_R' reflect the sample's (S-CQDs) and reference solution's (quinine sulphate) fluorescence quantum yields, respectively. The subscripts '*S*' and '*R*' represent the corresponding parameters for the S-CQDs (sample) and quinine sulphate (reference). 'Abs' denotes absorbance, '*A*' indicates the area beneath the fluorescence emission, and 'η' indicates the refractive index of the solvent (1.333 for water).

2.4.9. Time-resolved fluorescence spectroscopy. Time-resolved fluorescence emission decays were measured using a time correlated single photon counting (TCSPC) fluorometer equipment using the modular fluorescence lifetime system (DeltaFlex, HORIBA Scientific). The excitation source used was a 340 nm nano-LED pulse diode. The instrument response function (IRF) was measured utilizing a LUDOX®TMA colloidal silica, 34 wt% suspension in distilled water (Sigma-Aldrich), and the full-width at half-maximum (FWHM) was approximated to be about 200 ps. An emission monochromator was set at a fixed wavelength of 430 nm, with a bandpass of 16 nm.

For fluorescence lifetime measurements, the emission polarizer was set at the magic angle (54.7°) with respect to the excitation polarization. The time-resolved lifetime was measured over a 100-ns decay range, and the time per channel is 0.055 ns. To prevent any sample scattering, a long-pass filter was placed immediately after the sample. All decays were recorded at 25 °C and replotted with OriginPro 2021. The fluorescence emission decays were deconvoluted based on the instrument response function and then analyzed and fitted using the given equation.[52]

$$I(t) = \sum_i \alpha_i e^{-\frac{t}{\tau_i}} \quad (3)$$

where α_i and τ_i represent the contributions and lifetimes, respectively, of the different lifetime components, $I(t)$ represent the fluorescence intensity at time t. All data were collected at 25 °C. All the time-resolved fluorescence emission experiments were repeated three times.

2.4.10. Reproducibility of experimental methods. All chemicals utilized in this investigation were high purity and obtained from Loba Chemie, HiMedia and Sigma Aldrich. They have been used without any extra purification. The pH of the buffers was adjusted with a pH meter (EUTECH pH/Ion 510) to a final value of (±0.02) at ~24–25 °C. All the investigation has been undertaken using double-distilled water. Each time freshly synthesized S-CQDs were employed for the characterization and spectroscopic analyses, demonstrating the reproducible nature of the synthesis procedure. Although the HRTEM imaging was performed only once, efforts were made to capture images from several representative areas containing higher particle populations to analyze the particle size distribution. The histogram plot was subsequently obtained as described in Section 2.4.1. Further we have characterized the S-CQDs using XPS and EDS once to confirm the elemental composition and surface functionalization.

Additionally, GIXRD, zeta potential (ζ) measurements, and various spectroscopic techniques involving UV-visible, ATR FT-IR, steady-state and time-resolved fluorescence measurements were repeated at least three times each (please see the Experimental section). Error bars in the graphs represent the standard error of measurements obtained from three independent experiments.

3. Results and discussion

3.1. Morphological characterization and compositional analyses of S-CQDs

The morphology and size distribution of the as-prepared S-CQDs were examined using high-resolution transmission electron microscopy (HR-TEM). Fig. 1a displays homogeneous distribution of S-CQDs (nearly spherical). The histogram demonstrates a narrow size distribution of S-CQDs in the range of 1–5.4 nm, with an average diameter of 3.06 nm (Fig. 1a inset) displaying a strong resemblance to the Gaussian distribution. Fig. 1b depicts the FTIR spectra of SCQDs. The peak at 3355–3222 cm^{-1} is owing to the stretching vibrations of O–H and N–H functional groups, of S-CQDs wherein the broadening is attributed to hydrogen bonding.[54] The S-CQDs hydrophilicity

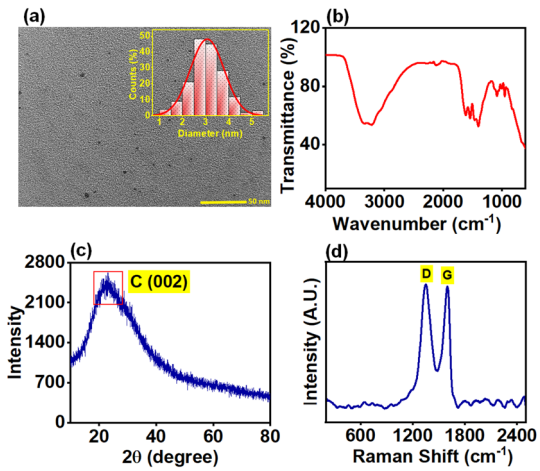

Fig. 1 (a) HR-TEM image of S-CQDs, inset shows particle size distribution histogram plot, (b) XRD spectrum, (c) FTIR spectrum and (d) energy dispersive spectroscopy (EDS) spectrum of S-CQDs representing various elements presence on the S-CQDs surface. The table (inset) displays the percentage composition of each element present in the S-CQDs.

and subsequent water dispersibility may be attributed to the presence of these bonds. The bands at 3034 cm^{-1}, are due to the stretching of –C–H. The absorption band at 2112 cm^{-1}, present only in S-CQDs, can be referred to as the triple bond stretching in groups –C≡C, and –C≡N.[55] The peak at 1624 cm^{-1} is also due to the N–H bending mode of the amine group coupled with the C–O. strong feature at 1398 cm^{-1} corresponds to the symmetric stretches of the carboxylate group.[56] Band at 1080 cm^{-1} were assigned to –C–O stretching.[57]

Furthermore, energy dispersive X-ray spectroscopy (EDS) is shown in Fig. S2† showing the presence of various elements like carbon, nitrogen, oxygen and chlorine in the synthesized S-CQD. The X-ray diffraction pattern of synthesized S-CQDs is shown in Fig. 1c. Strong wide diffraction peak was identified around $2\theta = 23°$ was credited to the as-prepared S-CQDs' (002) graphitic carbon lattice spacing, exhibiting an amorphous carbon phase on the S-CQDs surface which is in excellent line with previous literature descriptions.[58–60]

The interlayer distance (*d*-spacing) was calculated utilizing Bragg's equation:

$$n\lambda = 2d\sin\theta \quad (4)$$

where '*n*' is a positive integer representing the "order" of reflection, 'λ' signifies the incident X-ray wavelength ($\lambda = 1.5406$ Å), and the variable '*d*' that represents the spacing between the diffracting planes. The S-CQDs estimated *d*-spacing value was 0.39, corresponding to the (002) lattice plane.[61,62] The dissimilarity in the interlayer spacing between S-CQDs and bulk graphite (0.34 nm) indicates that the surface of S-CQDs is highly adorned with functional groups. Interlayer distance is powerfully influenced by the existence of the attached hydroxyl, carbonyl, and carboxylic acid groups. These functional groups can enhance interlayer distance.[63,64] The Raman spectrum is displayed in Fig. 1d. It shows two broad features, corresponding to the D (disorder) and G (graphite) bands, respectively, at 1350 cm^{-1} and 1605 cm^{-1}. In disordered graphite or glassy carbon, the D band is generated by the vibrations of carbon atoms with dangling bonds in the termination plane (A_{1g} vibrational mode), whereas the G band is associated with the graphite's E_{2g} mode and the vibration of sp^2-bonded carbon atoms in a two-dimensional hexagonal lattice. Overall, Raman findings demonstrated the presence of hybridized carbon defects in S-CQDs, specifically sp^3 (D band) and sp^2 (G band).[65,66] The intensity ratio of the D to G band (I_D/I_G) is 0.84, indicating moderate level of graphitization in S-CQDs.[67]

X-ray photoelectron spectroscopy (XPS) is a highly valuable technique for identifying elements, determining the oxidation state of a surface, and quantifying precisely the quantity (percentage) of each element. Fig. 2 displays the deconvoluted XPS spectra for the C 1s, O 1s, N 1s, and Cl 2p elements, together with the pie chart distribution and survey spectrum of the synthesized S-CQDs. The elemental carbon (68%), oxygen (15.7%), nitrogen (13.3%) and chlorine (2.9%) peaks emerged at 283.3, 530.8, 399.5, and 196.9 eV, respectively (Fig. 2a and b).[12,67,68] The C 1s deconvolution spectrum displays distinct peaks at 283.8, 285.1 and 287.5 which corresponds to the transitions involving the –C=C/–C–C, –C=N/–C=O, –O–C=O, respectively (Fig. 2c).[12] The deconvolution spectrum of O 1s displayed two binding energy peaks at 530.5, and 532 eV, owing to the –C=O and –C–OH/ –C–O–C groups, respectively (Fig. 2d).[12,69] The deconvolution spectra of N 1s revealed two peaks at 399.3 and 401.8 eV, attributed to the presence of –C–N–C (pyridine N) and –N–H (pyrrolic N) groups on the S-CQDs surface, respectively (Fig. 2e).[12] The deconvolution spectrum of Cl 2p showed two binding energy peaks at 196, and 197.7 eV, corresponding to the –C–Cl and –N–Cl groups, respectively (Fig. 2f).[12,69] The XPS results strongly correlate the conclusions drawn from the FTIR analysis. Furthermore, the existence of C,

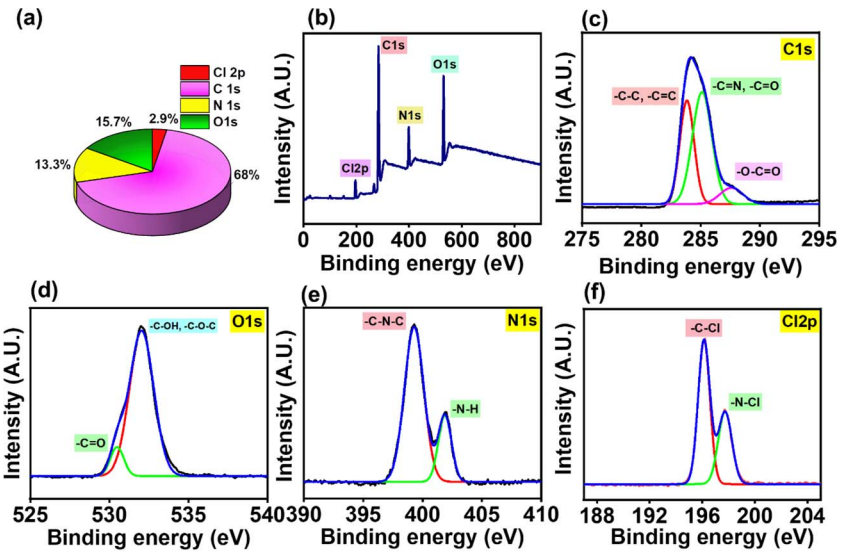

Fig. 2 (a) Pie chart represents exact elemental composition of S-CQDs from XPS analysis, (b) XPS survey spectrum of S-CQDs, (c–f) S-CQDs deconvoluted XPS spectra shown in an element-specific way *i.e.* (c) C 1s, (d) O 1s, (e) N 1s, and (f) Cl 2p.

O, N, and Cl elements in the S-CQDs was also verified using energy dispersive X-ray spectroscopy (EDS), shown in Fig. S2.†

3.2. Optimization of S-CQDs

To produce a high-performing optical nanosensor with powerful photoluminescent (PL) capabilities, it is crucial to fine-tune the response time, volume, and storage duration of the synthesized S-CQDs.

3.2.1. Reaction time and volume optimization. It is well-established that the reaction time influences the photoluminescence properties of S-CQDs. S-CQDs were synthesized with reaction periods ranging from 0.5 hour to 2.5 hours to determine the best reaction conditions. Our studies revealed that employing our hydrothermal technique, that entails a reaction spanning 2 hours at 200 °C, produces the desired S-CQDs with the most elevated photoluminescence intensity (Fig. S3a†).

In addition, volume adjustment is necessary for sensing efficiency as well as achieving the maximal fluorescence intensity of the produced nanoprobe. In order to optimize the volume, we observed the variations in the emission intensity of S-CQDs by gradually adding different quantities of aliquots (ranging from 10 to 60 μL) from the corresponding stock solution of S-CQDs into double-distilled water. The greatest photoluminescence (PL) intensity was observed when 30 μL of S-CQDs were mixed with 2.47 mL of double-distilled water, as shown in Fig. S3b.†

3.3. Optical properties of S-CQDs

Furthermore, the as-prepared S-CQDs demonstrate two discernible absorption bands at approximately 235 nm (π to π* transition, which corresponds to the C=C group of the potentially localized sp^2 clusters in carbon quantum dots) and 347 nm (n to π*) of the nitrogen and oxygen heteroatoms (C=N/C=O/N=O) present on the surface of S-CQDs as illustrated in UV-visible spectrum in Fig. 3a.[70–72] S-CQDs display a light brown to the unaided eye and green fluorescence emission when exposed to UV light at 365 nm (Fig. 3a inset). Furthermore, Fig. 3b displays the S-CQDs' excitation and emission spectra, having a λ_{em} at 341 nm and 455 nm, respectively.

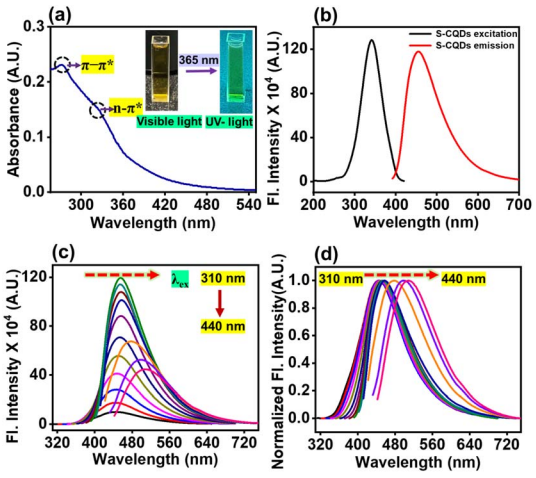

Fig. 3 (a) S-CQDs UV-visible absorption spectrum, with an inset image showing the S-CQDs under visible and UV light illumination, (b) excitation and emission spectrum of S-CQDs, (c) variations in fluorescence emission spectra of S-CQDs and (d) peak position-normalized fluorescence emission of S-CQDs plainly depicting the spectral shift, indicated by a dashed red arrow, from 443 nm to 508 nm (λ_{ex}: 310 nm to 440 nm).

S-CQDs demonstrated excitation wavelength-dependent emission spectra in aqueous media, with maximum emission intensity at 455 nm following excitation at 390 nm (Fig. 3c). The fluorescence emission of S-CQDs arises from the process of photoinduced charge separation and subsequent entrapment at the surface, leading to radiative recombination between hole and electron pairs.[73] The normalized fluorescence emission of S-CQDs is depicted in Fig. 3d. The fluorescence emission of S-CQDs exhibited a notable bathochromic shift of about 64 nm as the excitation wavelength was adjusted from 310 to 440 nm. The excitation-dependent emission characteristic of S-CQDs can be attributed to various factors, including the quantum confinement effect, zigzag sites, surface defects, aromatic structure formation on the surface, and non-uniform particle distribution.[54–56]

3.4. Stability of S-CQDs

Further we looked into the stability of S-CQDs by examining the effects of photo-irradiation, ionic strengths, and pH given its significance in real-world applications for a good and robust nanosensor.

S-CQDs exhibited exceptional stability within a pH range of 3 to 12, with minimal fluctuations in fluorescence emission intensity and no alteration in their emission maxima (Fig. 4a). Therefore, the synthesized S-CQDs can be effectively utilized as a versatile and durable pH sensor. The presence of numerous functional groups on the surface of the S-CQDs in an acidic environment result in a greater net surface charge (negative), which causes electrostatic repulsion and amplifies the slight increase in PL emission.

Additionally, S-CQDs were tested with a 0–1 M NaCl solution to determine the effect of ionic strength. Varying the ionic strength of the medium did not significantly alter the PL intensity or the emission maxima of S-CQDs, indicating that the nanoprobe is quite stable (Fig. 4b). The S-CQDs exhibit an intrinsic pH value of approximately 3.2, indicating their acidic character, likely attributed to the existence of carboxylates. In addition, the zeta potential value of S-CQDs (−9.37 mV) confirmed the presence of plenty of negatively charged components on the surface of S-CQDs (Fig. S3c†).

The fluorescence response of the CDs was examined for the temperature range of 10 to 90 °C (Fig. 4c), revealing a reduction in fluorescence with increasing temperature. The results reveal that S-CQDs have outstanding reversibility and recoverability across a temperature range of 10 to 90 °C. In other words, the temperature-dependent fluorescence of S-CQDs does not permanently degrade the surface fluorescent structures of the produced nanoprobe. A strong linear correlation ($R^2 = 0.99$) was

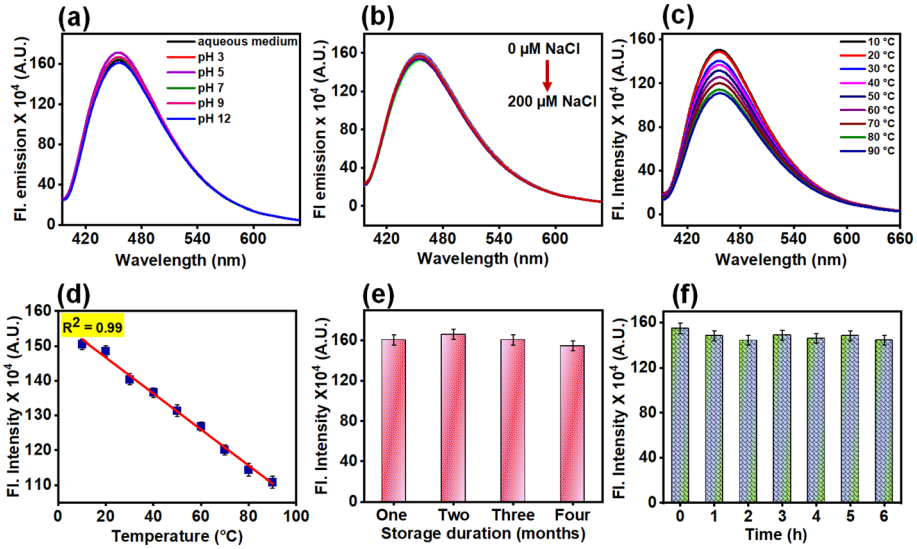

Fig. 4 (a) Fluorescence emission spectra of S-CQDs in aqueous medium at different solution pH (3, 5, 7, 9 12), (b) effect of medium's ionic strength on S-CQDs in the presence of variable concentrations of NaCl (0–200 μM), (c) impact of temperature variation on S-CQDs from 10–90 °C, (d) F_1. Intensity plot as function of temperature (10–90 °C). The red line indicates the linear fit of the data using OriginPro 2023 and R^2 denotes the goodness of the fits, and (e) fluorescence emission spectra of S-CQDs in aqueous medium at different storage time interval, (f) effect of photo-irradiation by a xenon arc lamp on the emission of S-CQDs at as a function of time. The error bars show the standard error of measurements taken from three different experiments.

observed between the temperature and the fluorescence intensity of the S-CQDs (Fig. 4d). Moreover, the peak position of the S-CQD emission at 445 nm remained constant across various temperatures. The discernible fall in fluorescence emission on temperature rise, could be due to CD aggregation or a synergistic interaction between the numerous oxygen-containing functional groups and hydrogen bonds. The phenomena can be attributed to the relaxation of photoexcited electrons, which can occur through radiative relaxation, non-radiative relaxation, and thermally activated traps on surfaces and impurity states throughout the heating process, as per earlier publications.[74–76]

The emission spectra of S-CQDs were measured at different time intervals over a period of 122 days, equivalent to 4 months. Fig. 4e displays the emission spectra of S-CQDs during different storage periods, revealing no noticeable alterations in the fluorescence intensity. Hence, the results unambiguously demonstrated that the synthesized nanoprobe exhibited exceptional stability in an aqueous solution over an extended period of time. Indeed, it might be beneficial in numerous analytical applications.

The photostability of the as-prepared S-CQDs was assessed by subjecting them to a 150 W xenon-arc lamp for six hours; however, no notable change in the fluorescence intensity of the S-CQDs was noted confirming its photostability and resistance to photobleaching (Fig. 4f).

3.5. Selectivity studies of S-CQDs

The evaluation of selectivity is a crucial factor in the development of an innovative nanosensor. To validate the selectivity of the analytical sensing platform, we observed the variations in fluorescence intensity of S-CQDs when exposed to various bioactive compounds (Fig. 5a), metal ions and pollutants (Fig. 5b). A specific concentration of various biomolecules (1 mM) was added to the aqueous solution of S-CQDs. Bioactive molecules include arginine (Arg), asparagine (Asn), aspartic acid (Asp), cysteine (Cys), glutamic acid (Glu), glutamine (Gln), histidine (His), isoleucine (Ile), leucine (Leu), lysine (Lys), methionine (Met), threonine (Thr), tyrosine (Tyr), and valine (Val), glutathione (gsh). Furthermore, metal ions and pollutants includes 4-nitrophenol (4-NP), 3-nitrophenol (3-NP), 2-nitrophenol (2-NP), ferric chloride hexahydrate ($FeCl_3 \cdot 6H_2O$), manganese(II) chloride tetrahydrate ($MnCl_2 \cdot 3H_2O$), lead nitrate [$Pb(NO_3)_2$], cobalt chloride hexahydrate ($CoCl_2 \cdot 6H_2O$), nickel(II) chloride hexahydrate ($NiCl_2 \cdot 6H_2O$), magnesium chloride hexahydrate ($MgCl_2 \cdot 6H_2O$), barium chloride dihydrate ($BaCl_2 \cdot 2H_2O$), ferrous chloride ($FeCl_2$), mercuric chloride ($HgCl_2$), picric acid (PA), ammonium chloride (NH_4Cl), copper chloride ($CuCl_2$), chromium(III) nitrate $Cr(NO_3)_3$, sodium arsenite (Na_3AsO_4) and thiourea (CH_4N_2S). Fig. 5b shows that 4-NP had the strongest fluorescence quenching of the S-CQDs, although the PL intensity of the S-CQDs remained practically unaltered upon addition of the remaining analytes. Therefore, it is inferred that our synthesized S-CQDs demonstrated exceptional selectivity as fluorescent nanosensor for 4-NP detection.

3.6. Plausible sensing mechanism for 4-NP detection

The subsequent titrations of S-CQDs were carried out by adding different concentrations of 4-NP (0–3.8 μM) in aqueous solution (Fig. 5c), and real samples of 4-NP (Fig. S4a†). The PL intensity of S-CQDs decreases progressively on gradual addition of 4-NP. Subsequently, a calibration curve was constructed by the plotting of fluorescence quenching efficiency ($F_0 - F/F_0$) against 4-

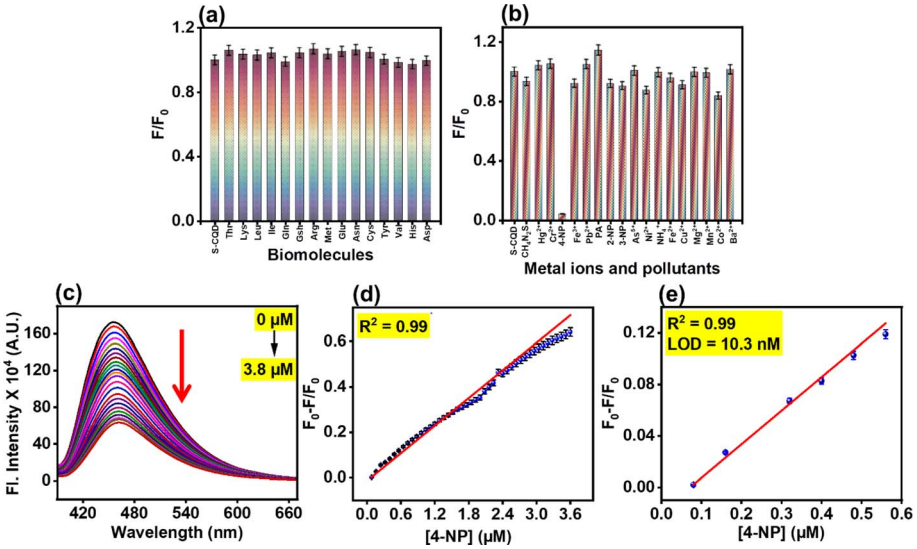

Fig. 5 Selectivity studies of S-CQDs with different (a) biomolecules, and (b) metal ions and pollutants. (c) Variation in fluorescence emission of S-CQDs in the presence of different concentrations of 4-NP (0–3.8 μM) red arrow depicts the progressive decrease of fl. intensity of S-CQDs, (d) the spectra depict linear correlation between $F_0 - F/F_0$ and different concentrations of 4-NP (0 to 3.8 μM), (e) the spectra show linear correlation between $F_0 - F/F_0$ and some specific concentrations of 4-NP (0 to 0.56 μM). Every steady-state fluorescence experiment was repeated at least three times. Error bars represent standard error of measurements obtained from three independent experiments.

NP concentration and a good linear fit was achieved with the good fit of adjusted R^2 value of 0.99 as shown in Fig. 5d and S4b.† Limit of detection was estimated to be 10.3 nM in aqueous solution (Fig. 5e), and 11.7 nM in real samples of 4-NP (Fig. S4c†), respectively. It should be highlighted that previously described fluorescent probes for 4-NP were produced using complicated, time-consuming, and energy-intensive methodologies. Moreover, S-CQDs exceptional fluorescence stability improves the analysis method's reliability and reproducibility. As a result, this study presents a simple, quick, sensitive, and low-cost technique for 4-NP sensing. There is multiple PL quenching mechanism which include Förster resonant energy

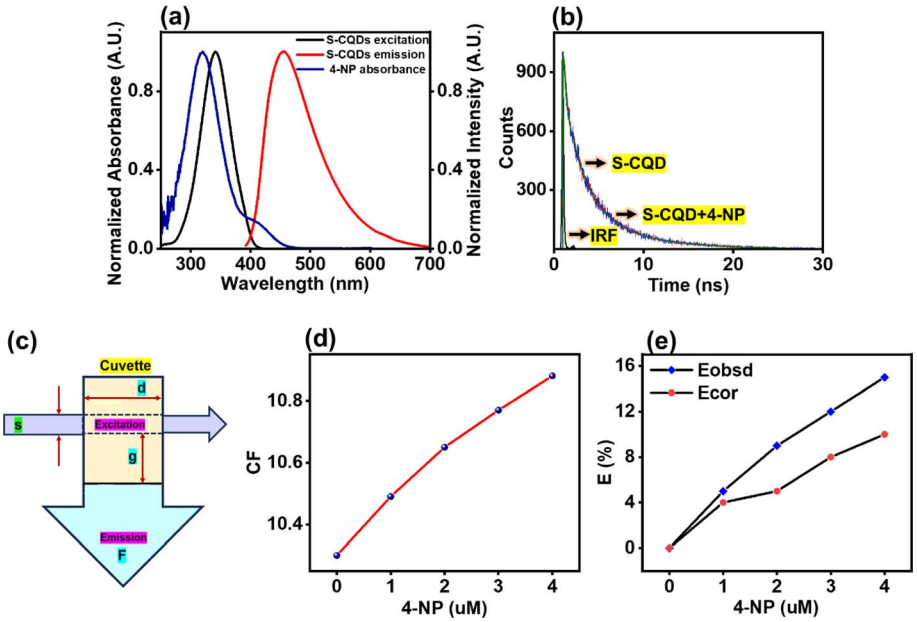

Fig. 6 (a) 4-NP absorption spectrum with S-CQD excitation and emission spectrum, (b) fluorescence lifetime decays of S-CQDs, where the sharp, thin black line represents the instrument response function, the red and magenta lines represent the actual intensity decays in the absence and presence of RF respectively. The wine and purple lines correspond to fits obtained in the absence and presence of RF, respectively using tri-exponential function (See eqn (3); Experimental section), (c) schematic representation of parameters used in eqn (5) *i.e.* Parker equation, (d) plot demonstrates the correction factor (CF) with various concentrations of 4-NP, (e) suppressed efficiency (E%) of the corrected (redline, E_{cor}) and observed (blackline, E_{obsd}) fluorescence intensities.

transfer (FRET), inner filter effect (IFE), and static or dynamic quenching.[52] The precise PL quenching process used by the as-prepared S-CQDs sensing system was thoroughly investigated. To investigate the potential fluorescence quenching mechanism of S-CQDs by 4-NP, the spectral overlap between the absorption spectrum of 4-NP and the fluorescence emission spectrum of S-CQDs was first considered. The absorption spectrum of 4-NP and the fluorescence emission spectrum of S-CQDs clearly overlapped suggesting that Inner filter effect (IFE) or Fluorescence resonance energy transfer (FRET) might have contributed to the fluorescence quenching (Fig. 6a).[77] In case of FRET, the probes' excited state energy transfer was responsible for the decrease in fluorescence lifespan.[78] Fluorescence quenching may occur with IFE, however the lifetime remains essentially unaltered.[77–80] To further confirm the quenching mechanism, the fluorescence lifetime of S-CQDs in the presence and absence of 4-NP was measured. As illustrated in Fig. 6b, the fluorescence lifetime of S-CQDs ($\tau = 2.24$ ns) is nearly identical to that of the S-CQDs-4-NP ($\tau = 2.07$ ns) sensing system illustrating absence of FRET, similar trend in lifetime values was observed in case of real sample of 4-NP (Fig. S4d†) confirming that the interaction happens solely *via* the IFE. These findings are consistent with previously published results based on IFE theory.[78]

Further FTIR data also shows the interactions. 3320–3192 cm^{-1} corresponds to the –NH/–OH stretching vibrations, peak around 1620 cm^{-1} corresponds to presence of –C=O stretching/–NH_2 bending, peaks around 1430 cm^{-1} and 1081 cm^{-1} bending vibrations of –CH_2 and –CH_3 groups as seen clearly in the DES (Choline chloride-urea) FTIR spectra (Fig. S6a†). From literature, it was found that only sucrose assisted CQDs has hydroxyl, carbonyl and epoxy functional groups.[6] Now in our case DES assisted SCQDs showed 3355–3222 cm^{-1} peak owing to the stretching vibrations of O–H and N–H functional groups, of S-CQDs wherein the broadening is attributed to hydrogen bonding.[54] The S-CQDs hydrophilicity and subsequent water dispersibility may be attributed to the presence of these bonds. The bands at 3034, are due to the stretching of –C–H. The absorption band at 2112 cm^{-1}, present only in S-CQDs, can be referred to as the triple bond stretching in groups –C≡C, and –C≡N.[55] The peak at 1624 cm^{-1} is also due to the N–H bending mode of the amine group coupled with the C–O. strong feature at 1398 cm^{-1} corresponds to the symmetric stretches of the carboxylate group.[56] Band at 1080 cm^{-1} were assigned to –C–O stretching.[57] Fig. S6b† clearly depicts the FTIR spectra of S-CQDs, DES, complex (S-CQDs-4-NP), which clearly confirms the impact of DES modified the surface functionalization of synthesized S-CQDs. Now when compared in FTIR spectra the peak of S-CQDs and DES with the FTIR peak of complex (S-CQDs-4NP) we clearly observe the broadening of peak appeared around 3368–3214 cm^{-1}, which clearly confirm that hydrogen bonding interactions between S-CQDs and the analyte (4-NP) leading to energy transfer and fluorescence quenching if S-CQDs by 4-NP. (Fig. S6†)

To establish the appropriate mechanism between the IFE and FRET, we tracked the zeta potential values, which are −9.06 and −4.21 mV for S-CQDs and 4-NP, respectively (Fig. S3c†). Given the fact that they are both negatively charged, it is unlikely that 4-NP will adsorb on S-CQDs surface *via* electrostatic interactions which clearly rules out the existence of FRET quenching mechanism.[81] The overlap of 4-NP absorption spectra with the excitation and emission spectra of S-CQDs results in a resonant energy transfer process (contact quenching). Because 4-nitrophenolate does not emit fluorescence, only C-dot fluorescence quenching was seen. The contact quenching may be achieved through the production of the zwitterionic spirocyclic Meisenheimer complex (Fig. 4), in which the negative charge may delocalize over the cyclohexadiene ring while the nitro group and the positive charge diffused over an iminium group. The nitro group and the cyclohexadiene ring carry the negative charge, whereas the iminium group carries the positive charge. Fluorescence quenching results from the

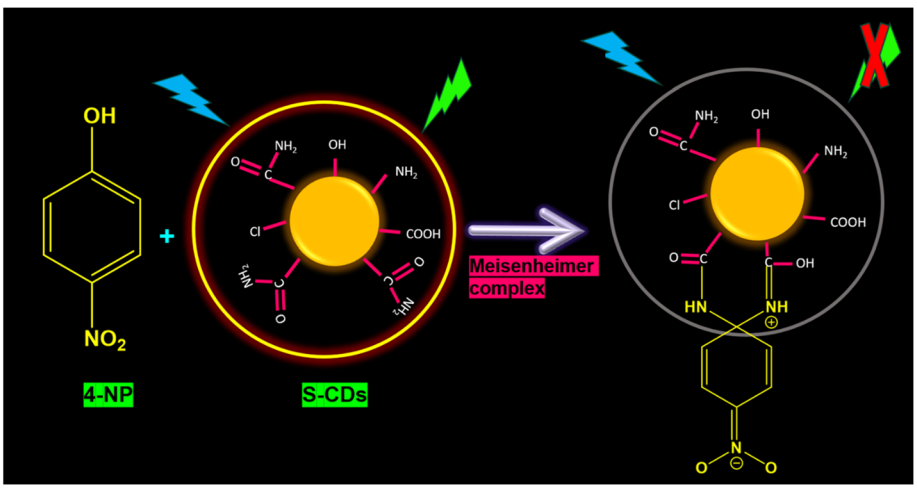

Scheme 2 Potential quenching mechanism of S-CQDs in the presence of 4-NP through formation of the zwitter ionic spirocyclic Meisenheimer complex.

Table 1 The different parameters employed to estimate IFE on the fluorescence quenching of S-CQDs by 4-NP

4-NP (μM)	A_{ex}	A_{em}	CF	F_{obsd}	F_{cor}	E_{obsd}	E_{cor}	$F_{cor}/F_{cor,0}$
0	0.034	0.009	10.30	454 260.8	4 678 241.3	0.00	0.00	1.00
1	0.051	0.01	10.40	430 039.3	4 511 106.4	0.05	0.04	0.96
2	0.065	0.011	10.65	415 299.7	4 421 695.1	0.09	0.05	0.95
3	0.077	0.013	10.77	400 323.1	733 677.2	0.12	0.08	0.92
4	0.086	0.014	10.88	388 196	4 221 768.9	0.15	0.10	0.90

transfer of energy caused by charge localization (Scheme 2).[79,80,82]

To further verify the hypothesis (IFE), corrections were made by taking into consideration the cell geometry and absorption properties of the 4-NPand S-CQDs aqueous solution with eqn (5) *i.e.* Parker equation:[80]

$$\frac{F_{cor}}{F_{obsd}} = \frac{2.3dA_{ex}}{1-10^{-dA_{ex}}}10^{gA_{em}}\frac{2.3sA_{em}}{1-10^{-sA_{em}}} \quad (5)$$

where A_{ex} and A_{em} correspond to the absorbances at the maximum excitation wavelength ($\lambda_{ex} = 390$ nm) and maximum emission wavelength ($\lambda_{em} = 455$ nm) respectively. F_{obsd} represents the measured fluorescence intensity of S-CQDs upon 4-NP addition at 455 nm. Removing IFE from F_{obsd} *via* eqn (5) yields the corrected fluorescence, or F_{cor}. The correction factor (CF) is represented as the ratio of F_{cor}/F_{obsd}. $E_{cor} = 1 - F_{cor}/F_{cor,0}$ where $F_{cor,0}$ and F_{cor} represents the corrected fluorescence intensities of S-CQDs in the absence and in the presence of 4-NP, respectively. As shown in Fig. 6c is the cuvette's width ($d = 1.00$ cm), g indicates the distance between the edge of the excitation beam to the edge of the cuvette ($g = 0.40$ cm) and s indicates the thickness of the excitation beam ($s = 0.10$ cm). The study of various parameters by using eqn (5) for the validation of the IFE was examined and is tabulated in Table 1.

The CF values were assessed at different 4-NP concentrations. The CF value was found to increase with an increase in the concentration of 4-NP (Fig. 6d), which agrees to the Parker equation (eqn (5)). The drop in photoluminescence (PL) emission of S-CQDs due to the addition of 4-NP was measured using a PL spectrophotometer. The corresponding corrected values were investigated as well (Fig. 6e). The value of E was determined using the equation: $E = 1 - F/F_0$, where F_0 and F represents the PL intensity of S-CQDs without and with addition of 4-NP, respectively. Hence, suppression of the PL intensity of S-CQDs is significantly influenced by the IFE.[80–82]

3.7. Determination of limit of detection

The characteristics for the ideal nanosensors sensitivity are included in the limit of detection (LOD) and limit of quantification (LOQ). A linear plot between PL responses ($F_0 - F/F$) and various concentrations of 4-NP was used to compute the LOD and LOQ values of the S-CQDs@4-NP nanosensor in aqueous medium and real sample of 4-NP (Table 2) using the values of ($3\sigma/K$) and ($10\sigma/K$), respectively.[78] The variable 'σ' represents the standard deviation of the intercept and 'K' is the slope of the respective graphs.[83,84] The experiment was repeated at least three times. Error bars represent standard error of measurements obtained from three independent experiments. The LOD values of 4-NP in presence of aqueous and real samples was found to be ~10.3 nM (Fig. 5e) and ~11.7 nM (Fig. S4b†), respectively with a linear concentration range of 0–3.8 μM along with excellent regression coefficient value of $R^2 = 0.99$. Table 3 shows that the developed nanosensor has a relatively lower detection limit and a high sensitivity when compared to other nanosensors described in the literature.

3.8. Determination of photophysical characteristics

As already shown, S-CQDs have outstanding fluorescence. Eqn (2) was used to estimate the PLQY of S-CQDS, and the result was ~56%, confirming that the nanoprobe in its prepared state is a bright fluorophore. The Stern–Volmer quenching constants were calculated (Table 2) using the following equation in order to understand the degree of quenching efficiency of S-CQDs.[7,52,85,86]

$$\frac{F_0}{F} = 1 + K_{SV}[Q] \quad (6)$$

Fig. S7† illustrates a graph between F_0/F and Q. The variables 'F_0' and 'F' represents the fluorescence intensity in the absence

Table 2 Analytical performance statistics for S-CQD-based 4-NP sensing[a]

Parameters	S-CQDs + 4-NP in aqueous medium	S-CQDs + 4-NP real sample
Linearity range (μM)	0–4	0–4
Limit of detection (LOD) (nM)	10.3	11.7
Limit of quantification (LOQ) (nM)	19.6	178.7
Binding constant (K_1) (μM^{-1})	4.93×10^5	3.33×10^5
Quenching constant (K_{sv}) (μM^{-1})	0.26	0.26
Regression coefficient (R^2)	0.99	0.99

[a] Error limit = ± 5%.

Table 3 Comparative evaluation of LOD for 4-NP detection using different nanosensors

Precursors	Method employed	Fluorescent probe	Detection limit (linear range)	Ref.
Glucose	Microwave-assisted method 900 W, 10 min	Carbon quantum dots (CQDs)	0.03 μM (0.1–2.5 μM)	44
Natural celery leaves and glutathione	Hydrothermal synthesis, 200 °C, 4 h	Carbon dots (CDs)	26 nM (0–1000 μM)	1
O-Phenylenediamine and dicyandiamine	Hydrothermal synthesis, 200 °C, 9 h	Nitrogen-doped carbon dots (N-CDs)	50 nM (0.1–39 μM)	45
Cuttlefish ink	Hydrothermal synthesis 180 °C, 12 h	Nitrogen and sulphur doped carbon quantum dots (N,S-CQDs)	0.05 μM (1.25–50 μM)	43
Polyethylene glycol 400 (PEG-400), sublimed sulfur powder, sodium hydroxide	72 h in an oil bath, 70 °C, 72 h	Sulphur quantum dots	70 nM (0.2–30 μM, 30–90 μM)	40
Triflic acid, palm shell	Microwave oven, 150 °C, 10 h	Nitrogen and sulphur co-doped CQDs	79 nM (0.2–0.40 μM)	46
Ethanediamine, copper(II) chloride dihydrate	Hydrothermal synthesis, 180 °C, 10 h	Cu-doped carbon dots (Cu-CDs)	80 nM (0.5–50 μm)	42
Maleic acid and ethylenediamine	Hydrothermal synthesis 190 °C, 15 h	Nitrogen-doped carbon quantum dots (N-CDs)	158 nM (0.10–11 μg mL^{-1})	49
A. auricula, diammonium hydrogen phosphate, ethylenediamine	Hydrothermal synthesis, 240 °C, 24 h	Nitrogen and phosphorus-doped carbon dots (Aa N,P-CDs)	198 nM (0–37.5 μM)	41
3-Aminophenylboronic acid monohydrate (3-APBA·H_2O)	Hydrothermal synthesis, 160 °C, 8 h	Boron and nitrogen co-doped carbon dots (B, N-CDs)	0.2 μM (0.5–60 μM)	87
Citric acid and urea	Hydrothermal synthesis, 180 °C, 60 min	Nitrogen-doped oxidized carbon dots (NOCDs)	2 μM (2–100 μM)	51
Giloy (*T. cordifolia*) stem	Hydrothermal synthesis, 160 °C, 5 h	N,S-doped CDs (N,S-CDs)	380 nM (0.5 to 230 μM)	48
Ethylene glycol and β-alanine	Heating 170 °C, 30 min	Nitrogen-doped carbon dots (NCDs)	0.4 μM (1–250 μM)	88
Sucrose and choline chloride and urea deep eutectic solvent	**Hydrothermal synthesis, 200 °C, 2 h**	**S-CQDs**	**10.3 nM (0–0.56 μM)**	**This work**

and presence of 4-NP, respectively and [Q] is concentration of the quencher *i.e.* 4-NP. 'K_{sv}' indicates Stern–Volmer quenching constant, which was computed from the slope of the plots in aqueous as well as in real sample. K_{sv} values reveals that the degree of S-CQD quenching is consistent regardless of 4-NP source. Furthermore, by applying the 1 : 1 linear Benesi–Hildebrand equation, the excited-state binding constant was determined (Table 2) to estimate the S-CQD-4-NP stoichiometry and comprehend the extent of interaction and binding in S-CQDs and 4-NP.[81]

$$\frac{1}{F_0 - F} = \frac{1}{F_0 - F_1} + \frac{1}{K_1[4 - \mathrm{NP}](F_0 - F)} \quad (7)$$

'F_0' and 'F_1' represents the fluorescence intensity of S-CQDs and S-CQDs-4-NP complex respectively. The plot of $(1/F_0 - F)$ against 1/[4-NP] gives a straight line (Fig. S8†). The binding constants (K_1) of the S-CQDs-4-NP complex were assessed in aqueous and real samples of 4-NP from the reciprocal of the corresponding slope values, as shown in Table 2. Overall, the binding constant (K_1) as well as LOD of S-CQDs and 4-NP appears to be similar irrespective of the source of 4-NP (Table 2) confirming our nanoprobe suitability and efficacy for 4-NP detection in real samples.

3.9. Selectivity of fluorescence assay

Various metal ions and biomolecules were also used to investigate the selectivity of the nanosensor (S-CQDs) for 4-NP detection (Fig. S5a and b†) as the potential interfering substances. None of the metal ions (1 mM) had any effect on the fluorescence intensity of S-CQDs in the presence and absence of 4-NP. Therefore, high tolerance to metal ions could be the basis for detecting 4-NP in water samples. The fluorescence quenching of S-CQDs by 4-NP in the presence of competitive compounds (1 mM) remained similar indicating the high selectivity of the sensor for detecting 4-NP.

3.10. Method reliability with real sample of 4-NP

It remains a challenging task to analyze the real samples for a presented fluorescent sensor, owing to the presence of potentially unknown interferents in real samples. The proposed nanosensor model was validated in accordance with ICHQ2(R1) recommendations.[89] We used the synthesized S-CQDs to

identify 4-NP in the river water samples in order to monitor the sensor's viability. The samples were spiked with varying doses of 4-NP. In the real sample, the LOD value was found to be ~11.7 nM (Fig. S4b†) with good recovery percentages and a relative standard deviation (RSD) as shown in Table S3.† Findings clearly suggest that our method is accurate, repeatable, and has good recovery rates. According to the aforementioned findings, the sensor offers a great potential for 4-NP detection in real world samples.

4. Conclusion

In summary, a quick, one-step hydrothermal technique was used to synthesize S-CQDs from sucrose that was both cost effective and environmentally friendly. The production of intrinsically functionalized and extremely luminous S-CQDs (PLQY 56%) without the use of harsh chemicals was made possible by a deep eutectic solvent. The nitrogen and chlorine functionalization of S-CQDs was validated using EDS, XPS, and FTIR, and their optical characteristics were studied using UV-visible, fluorescence, and time-resolved emission spectroscopy. S-CQDs demonstrated exceptional photostability and environmental stability (pH, ionic strength), as well as aqueous solubility fulfilling all the criteria for an ideal nanosensor that can be used in various fields. The as-prepared nanoprobe demonstrated selectivity and sensitivity to 4-NP detection in the nanomolar range *via* an inner filter effect mechanism. In addition, the proposed nanosensor model was validated on real sample of 4-NP at a nanomolar level with excellent accuracy and precision. While this nanoprobe has great potential for sensing, it is not without limitations. S-CQDs extreme selectivity towards 4-NP restricts its sensing ability towards other environmentally-toxic pollutants. Furthermore, S-CQDs must be handled carefully as their small size and high surface area renders them susceptible to contamination affecting its sensing selectivity and accuracy. This research paves the way for the development of a simple, eco-friendly, cost-effective, and highly selective fluorescent nanosensor for the rapid, on-site detection of 4-NP. This sensor provides a quicker and more effective way to check water quality than conventional techniques thanks to its nanomolar detection limits. Further, nanoprobes can be utilized in industrial operations and wastewater treatment to measure 4-NP levels, aiding in water pollution prevention. The potential to detect 4-NP quickly and sensitively aids in the development of effective pollution management and environment cleanup solutions.

Data availability

The data will be made available on request.

Conflicts of interest

The authors affirm that they have no known financial or interpersonal conflicts that would have appeared to have an impact on the research presented in this study.

Acknowledgements

M. K. is thankful to Thapar Institute of Engineering and Technology, Patiala for the fellowship and infrastructural facilities. We gratefully acknowledge financial assistance from the Science and Engineering Research Board (SERB) for the SRG grant to B. M. (SRG/2022/000942) as well as TIET, Patiala for seed money grant to B. M. We are also grateful to CIL, Panjab University, Chandigarh for HR-TEM analysis, IIT Ropar for XPS analysis facility and SPMS Thapar University for XRD and EDS analysis facility. The authors acknowledge Prof. Vijay Luxami and Ms. Aastha Palta for allowing us to use the TCSPC instrument.

References

1 K. Wang, L. Tan, Y. Zhang, D. Zhang, N. Wang and J. Wang, *Mar. Pollut. Bull.*, 2023, **187**, 114587–114595, DOI: **10.1016/j.marpolbul.2023.114587**.
2 Y. Tang, R. Huang, C. Liu, S. Yang, Z. Lu and S. Luo, *Anal. Methods*, 2013, **5**, 5508–5514, DOI: **10.1039/C3AY40742J**.
3 S. W. Huang, Y. F. Lin, Y. X. Li, C. C. Hu and T. C. Chiu, *Molecules*, 2019, **24**(9), 1785–1796, DOI: **10.3390/molecules24091785**.
4 K. B. Narayanan and N. Sakthivel, *J. Hazard. Mater.*, 2011, **189**, 519–525, DOI: **10.1016/j.jhazmat.2011.02.069**.
5 V. A. Ansi and N. K. Renuka, *Mater. Today: Proc.*, 2019, **18**, 1724–1728, DOI: **10.1016/j.matpr.2019.05.269**.
6 V. A. Ansi, P. Sreelakshmi, P. Raveendran and N. K. Renuka, *Mater. Res. Bull.*, 2021, **129**, 111284–111288, DOI: **10.1016/j.materresbull.2021.111284**.
7 A. Kundu, J. Brar, A. Mishra, B. Maity and S. Basu, *Mater. Adv.*, 2025, **6**, 743–755, DOI: **10.1039/D4MA00925H**.
8 F. Wang, M. Kreiter, B. He, S. Pang and C. Y. Liu, *Chem. Commun.*, 2010, **46**, 3309–3311, DOI: **10.1039/C002206C**.
9 S. Liu, T. Quan, L. yang, L. Deng, X. Kang, M. Gao, Z. Xia, X. Li and D. Gao, *ACS Omega*, 2021, **6**, 29022–29036, DOI: **10.1021/acsomega.1c04078**.
10 Q. Zhang, K. D. O. Vigier, S. Royer and F. Jérôme, *Chem. Soc. Rev.*, 2012, **41**, 7108–7146, DOI: **10.1039/C2CS35178A**.
11 S. Khare, N. Sohal, M. Kaur and B. Maity, *Heliyon*, 2025, **11**, e41853, DOI: **10.1016/j.heliyon.2025.e41853**.
12 N. Wang, A. Q. Zheng, X. Liu, J. J. Chen, T. Yang, M. Chen and J. H. Wang, *ACS Appl. Mater. Interfaces*, 2018, **10**, 7901–7909, DOI: **10.1021/acsami.8b00947**.
13 X. Jiang, Y. Shi, X. Liu, M. Wang, P. Song, F. Xu and X. Zhang, *Polymers*, 2018, **10**, 1282, DOI: **10.3390/polym10111282**.
14 J. Song, N. Zhao, Y. Qu and L. Zhao, *Dyes Pigm.*, 2021, **193**, 109564, DOI: **10.1016/j.dyepig.2021.109564**.
15 Y. Shen, H. Zhou, X. He, F. Shen, Z. Xu, B. Yang, L. Kong and L. Dai, *Green Chem.*, 2024, **26**, 8123–8144, DOI: **10.1039/D4GC01579G**.
16 N. Wang, A. Q. Zheng, X. Liu, J.-J. Chen, T. Yang, M.-L. Chen and J.-H. Wang, *ACS Appl. Mater. Interfaces*, 2018, **10**(9), 7901–7909, DOI: **10.1021/acsami.8b00947**.

17 Y. Tang, S. Shang, J. Yang, B. Lü, F. Peng, W. Huan and J. Bian, *Ind. Crops Prod.*, 2025, **224**, 120440, DOI: 10.1016/j.indcrop.2024.120440.
18 R. Tabaraki and F. Nazari, *J. Photochem. Photobiol., A*, 2023, **444**, 114891, DOI: 10.1016/j.jphotochem.2023.114891.
19 S. Cailotto, E. Amadio, M. Facchin, M. Selve, E. Pontoglio, F. Rizzolio, P. Riello, G. Toffoli, A. Benedetti and A. Perosa, *ACS Med. Chem. Lett.*, 2018, **9**, 832–837, DOI: 10.1021/acsmedchemlett.8b00240.
20 Y. A. Alomair and S. M. Holmes, *RSC Adv.*, 2019, **9**, 10437, DOI: 10.1039/c9ra01312a.
21 B. Appiagyei, D. A. Anang, J. O. Bonsu, L. A. Ahenkorah, S. D. Mane, H.-S. Kim and C. Bathula, *J. Electroanal. Chem.*, 2023, **936**, 117383, DOI: 10.1016/j.jelechem.2023.117383.
22 S. Treepet, C. Chokradjaroen, K. Kim, N. Saito and A. Watthanaphanit, *Mater. Today Chem.*, 2022, **26**, 101139, DOI: 10.1016/j.mtchem.2022.101139.
23 N. Nammahachak, K. K. Aup-Ngoen, P. Asanithi, M. Horpratum, S. Chuangchote, S. Ratanaphan and W. Surareungchai, *RSC Adv.*, 2022, **12**, 31729–31733, DOI: 10.1039/D2RA05989D.
24 L. Tang, R. Ji, X. Li, K. S. Teng and S. P. Lau, *Part. Part. Syst. Charact.*, 2013, **30**, 523–531, DOI: 10.1002/ppsc.201200131.
25 H. K. Sadhanala, J. Khatei and K. K. Nanda, *RSC Adv.*, 2014, **4**, 11481–11485, DOI: 10.1039/C3RA47527A.
26 A. P. Abbott, D. Boothby, D. L. Davies and R. K. Rasheed, *J. Am. Chem. Soc.*, 2024, **126**, 9142–9147, DOI: 10.1021/ja048266j.
27 M. Jablonsky and J. Sima, *BioResources*, 2022, **17**, 3880–3882, DOI: 10.15376/biores.17.3.3880-3882.
28 G. L. P. Rao, A. Mandal and N. Pal, *Chem. Phys.*, 2025, **588**, 112496, DOI: 10.1016/j.chemphys.2024.112496.
29 O. S. Hammond, D. T. Bowronb and K. J. Edler, *Green Chem.*, 2016, **18**, 2736–2744, DOI: 10.1039/C5GC02914G.
30 J. A. Sirviö, M. Visankob and H. Liimatainena, *Green Chem.*, 2015, **17**, 3401–3406, DOI: 10.1039/C5GC00398A.
31 D. Nguyen, T. V. Huynh, V. S. Nguyen, P.-L. D. Cao, H. T. Nguyen, T.-C. Wei, P. H. Tran and P. T. Nguyen, *RSC Adv.*, 2021, **11**, 21560–21566, DOI: 10.1039/d1ra03273a.
32 A. Prabhune and R. Dey, *J. Mol. Liq.*, 2023, **379**, 121676, DOI: 10.1016/j.molliq.2023.121676.
33 Y. Ma, Y. Yang, T. Li, S. Hussain and M. Zhu, *Green Chem.*, 2024, **26**, 3627–3669, DOI: 10.1039/D3GC04289H.
34 I. H. Naser, H. T. A. Alamir, A. H. Al-Shukarji, B. A. Ahmed, T. A. Qassem, M. Kamal, T. M. Almeleebia, E. R. Alwaily and E. Hasan, *Front. Chem.*, 2024, **12**, 1342784–1342802, DOI: 10.3389/fchem.2024.1342784.
35 Z. Wang, X. Zhao, Y. Chen, C. Wei and J. Jiang, *RSC Sustain.*, 2025, **3**, 738–756, DOI: 10.1039/D4SU00560K.
36 C. Pinghua, S. Yangming, N. Pingping, W. Tao, L. Xueqin, J. Hualin, Z. Weiqiang, S. Hongying, C. Jiezeng and T. Enzhu, *J. Taiwan Inst. Chem. Eng.*, 2019, **97**, 128–136, DOI: 10.1016/j.jtice.2018.12.023.
37 Y. Wang, R. Wu, Y. Zhang, S. Cheng, B. Wang, Y. Zhang and Y. Zhang, *Spectrochim. Acta, Part A*, 2024, **308**, 123709–123719, DOI: 10.1016/j.saa.2023.123709.
38 G. Guo, T. Li, Z. Liu, X. Luo, T. Zhang, S. Tang, X. Wang and D. Chen, *Food Chem.*, 2024, 137232–137241, DOI: 10.1016/j.foodchem.2023.137232.
39 L. Yang, Y. Cui, B. Hu and X. Xu, *ACS Appl. Nano Mater.*, 2024, 7(5), 5146–5155, DOI: 10.1021/acsanm.3c05916.
40 X. Peng, Y. Wang, Z. Luo, B. Zhang, X. Mei and X. Yang, *Microchem. J.*, 2021, **170**, 06735–106742, DOI: 10.1016/j.microc.2021.106735.
41 Y. Tu, S. Wang, X. Yuan, P. Song, Y. Wei, K. Qin, Q. Zhang and X. Ji, *Anal. Methods*, 2020, **12**, 2237–2243, DOI: 10.1039/D0AY00316F.
42 J. Fang, S. Zhuo and C. Zhu, *Opt. Mater.*, 2019, **97**, 109396–109402, DOI: 10.1016/j.optmat.2019.109396.
43 X. Huang, C. Yang, Y. Chen, Z. Zhu and L. Zhou, *Anal. Methods*, 2021, **13**, 5351–5359, DOI: 10.1039/D1AY01496J.
44 M. Amjadi and T. Hallaj, *J. Lumin.*, 2016, **171**, 202–207, DOI: 10.1016/j.jlumin.2015.11.019.
45 M. Tian, Y. Liu, Y. Wang and Y. Zhang, *Spectrochim. Acta, Part A*, 2019, **220**, 117117–117124, DOI: 10.1016/j.saa.2019.05.022.
46 H. Soni and P. S. Pamidimukkala, *Mater. Res. Bull.*, 2018, **108**, 250–254, DOI: 10.1016/j.materresbull.2018.08.033.
47 S. Swain and A. K. Jena, *ACS Omega*, 2025, **10**(6), 5874–5885, DOI: 10.1021/acsomega.4c09748.
48 H. Yuan, J. Yu, S. Feng and Y. Gong, *RSC Adv.*, 2016, **6**, 15192–15200, DOI: 10.1039/C5RA26870B.
49 Y. Qu, L. Yu, B. Zhu, F. Chai and Z. Su, *New J. Chem.*, 2020, **44**, 1500–1507, DOI: 10.1039/C9NJ05285B.
50 N. K. R. Bogireddy, R. C. Silva, M. A. Valenzuela and V. Agarwal, *J. Hazard. Mater.*, 2020, **386**, 121643, DOI: 10.1016/j.jhazmat.2019.121643.
51 S. M. Roopan, S. H. Prakash, R. Manjupriya, M. S. Hasan, F. Afridha, A. Rajesh, R. Sneha, P. V. Kumar and M. Shobika, *Biomass Convers. Biorefin.*, 2024, DOI: 10.1007/s13399-024-05422-7.
52 J. R. Lakowicz, *Principles of Fluorescence Spectroscopy*, Springer, New York, 3rd edn, 2006, vol. 1–95, pp. 529–575.
53 A. T. R. Williams, S. A. Winfield and J. N. Miller, *Analyst*, 1983, **108**, 1067–1071, DOI: 10.1039/an983080106729.
54 H. L. Yang, L. F. Bai, Z. R. Geng, H. Chen, L. T. Xu, Y. C. Xie, D. J. Wang, H. W. Gu and X. M. Wang, *Mater. Today Adv.*, 2023, **18**, 100376–100400, DOI: 10.1016/j.mtadv.2023.100376.
55 S. E. Elugoke, G. E. Uwaya, T. W. Quadri and E. E. Ebenso, *ACS Symp. Ser.*, **1465**, 3–42, DOI: 10.1021/bk-2024-1465.ch001.
56 A. B. Siddique, S. M. Hossain, A. K. Pramanick and M. Ray, *Nanoscale*, 2021, **13**, 16662–16671, DOI: 10.1039/D1NR04301C.
57 B. L. Rossi, C. M. B. Andrade, E. M. Therézio, R. J. Ramos, L. G. Vasconcelos, A. J. Terezo and A. B. D. Siqueira, *Front. Chem.*, 2022, **10**, 858323–858337, DOI: 10.3389/fchem.2022.858323.
58 A. Tadesse, D. RamaDevi, M. Hagos, G. Battu and K. Basavaiah, *RSC Adv.*, 2018, **8**, 8528–8536, DOI: 10.1039/C8RA00158H.

59 B. rooj and U. Mandal, *Vietnam J. Chem.*, 2023, **61**, 693–718, DOI: 10.1002/vjch.202300022.
60 A. Pal, M. P. Sk and A. Chattopadhyay, *Mater. Adv.*, 2020, **1**, 525, DOI: 10.1039/d0ma00108b.
61 N. Kazemifard, A. A. Ensafi and B. Rezaei, *Food Chem.*, 2020, **310**, 125812–125820, DOI: 10.1016/j.foodchem.2019.125812.
62 L. Li, G. Wu, G. Yang, J. Peng, J. Zhao and J. J. Zhu, *Nanoscale*, 2013, **5**, 4015–4039, DOI: 10.1039/C3NR33849E.
63 T. Selvakumar, M. Rajaram, A. Natarajan, L. Harikrishnan, K. Alwar and A. Rajaram, *ACS Omega*, 2022, **7**, 12825–12834, DOI: 10.1021/acsomega.2c00092.
64 V. Raveendran, A. R. S. Babu and N. K. Renuka, *RSC Adv.*, 2019, **9**, 12070–12077, DOI: 10.1039/C9RA02120E.
65 X. Maa, S. Lia, V. Hesselb, L. Linc, S. Meskersc and F. Gallucci, *Chem. Eng. Process.*, 2019, **140**, 29–35, DOI: 10.1016/j.cep.2019.04.017.
66 T. Palaniselvam, H. B. Aiyappa and S. Kurungot, *J. Mater. Chem.*, 2012, **2**, 23799–23805, DOI: 10.1039/C2JM35128E.
67 P. Krishnaiah, R. Atchudan, S. Perumal, P. Gangadaran, D. Manoj, B. C. Ahn, R. S. Kumar, A. I. Almansour, Y. R. Lee and B. H. Jeon, *Spectrochim. Acta, Part A*, 2024, **304**, 123422–123431, DOI: 10.1016/j.saa.2023.123422.
68 M. Wang, C. Li, M. Zhou, Z. Xia and Y. Huang, *Green Chem.*, 2022, **24**, 6696–6706, DOI: 10.1039/D2GC01949C.
69 Y. Xie, D. Cheng, X. Liu and A. Han, *Sensors*, 2019, **19**, 3169–3179, DOI: 10.3390/s19143169.
70 S. H. Chiua, G. Geddaa, W. M. Girmaa, J. Chenb, Y. C. Lingc, A. Ghuled, K. Oue and J. Chang, *Acta Biomater.*, 2016, **46**, 151–164, DOI: 10.1016/j.actbio.2016.09.027.
71 A. Das, E. V. Kundelev, A. A. Vedernikova, S. A. Cherevkov, D. V. Danilov, A. V. Koroleva, E. V. Zhizhin, A. N. Tsypkin, A. P. Litvin, A. V. Fedorov, E. V. Ushakova and A. L. Rogach, *Light Sci. Appl.*, 2022, **11**, 1–13, DOI: 10.1038/s41377-022-00778-9.
72 S. K. Singh, A. Srinivasan, S. Mitra and P. S. G. Pattader, *Spectrochim. Acta, Part A*, 2022, **271**, 120906–120919, DOI: 10.1016/j.saa.2022.120906.
73 W. You, W. Zou, S. Jiang, J. Zhang, Y. Ge, G. Lu, D. W. Bahnemann and J. H. Pan, *Carbon Neutralization*, 2023, **3**, 245–284, DOI: 10.1002/cnl2.120.
74 H. Zhang, J. You, J. Wang, X. Dong, R. Guan and D. Cao, *Dyes Pigm.*, 2020, **173**, 107950–107980, DOI: 10.1016/j.dyepig.2019.107950.
75 X. Cui, Y. Wang, J. Liu, Q. Yang, B. Zhang, Y. Gao, Y. Wang and G. Lu, *Sens. Actuators, B*, 2017, **242**, 1272–1280, DOI: 10.1016/j.snb.2016.09.032.
76 S. Dua, P. Kumar, B. Pani, A. Kaur, M. Khanna and G. Bhatt, *RSC Adv.*, 2023, **13**, 13845–13861, DOI: 10.1039/D2RA07180K.
77 J. Zhang, R. Zhou, D. Tang, X. Hou and P. Wu, *Trends Anal. Chem.*, 2019, **110**, 183–190, DOI: 10.1016/j.trac.2018.11.002.
78 A. Kundu, B. Maity and S. Basu, *ACS Omega*, 2023, **8**, 22178–22189, DOI: 10.1021/acsomega.3c02474.
79 R. F. Bogale, Y. Chen, J. Ye, Y. Yang, A. Rauf, L. Duan, P. Tian and G. Ning, *Sens. Actuators, B*, 2017, **245**, 171–178, DOI: 10.1016/j.snb.2017.01.177.
80 W. Li, H. Zhang, S. Chen, Y. Liu, J. Zhuang and B. Lei, *Biosens. Bioelectron.*, 2016, **86**, 706–713, DOI: 10.1016/j.bios.2016.07.034.
81 N. Sohal, B. Maity and S. Basu, *ACS Appl. Bio Mater.*, 2022, **5**, 2355–2364, DOI: 10.1021/acsabm.2c00189.
82 G. H. G. Ahmed, R. B. Laíño, J. A. G. Calzón and M. D. E. García, *Microchim. Acta*, 2015, **182**, 51–59, DOI: 10.1007/s00604-014-1302-x.
83 M. Kaur, M. Bhattacharya and B. Maity, *RSC Sustainability*, 2024, 1472–1486, DOI: 10.1039/D3SU00456B.
84 M. Kaur, N. Sohal, M. Phull and B. Maity, *RSC Appl. Interfaces*, 2024, **1**, 1174–1185, DOI: 10.1039/D4LF00143E.
85 K. Sekioka, N. Mosleh, D. Boice, R. Hailstone and X. Sun, *Mater. Adv.*, 2025, **6**, 2875–2884, DOI: 10.1039/D5MA00021A.
86 A. Kundu, B. Maity and S. Basu, *ACS Biomater. Sci. Eng.*, 2022, **8**(11), 4764–4776, DOI: 10.1021/acsbiomaterials.2c00798.
87 N. Xiao, S. G. Liu, S. Mo, N. Li, Y. Jun Ju, Y. Ling, N. B. Li and H. Q. Luo, *Talanta*, 2018, **184**, 184–192, DOI: 10.1016/j.talanta.2018.02.114.
88 D. Das and R. K. Dutta, *ACS Appl. Nano Mater.*, 2021, **4**(4), 3444–3454, DOI: 10.1021/acsanm.0c03329.
89 Guideline, ICHHT, *Validation of Analytical Procedures: Text and Methodology, Q2*, 2005, vol. **1**, p. 20.